Supplementary Information for

Sphere of arbitrarily polarized exceptional points with a single planar metasurface

Haoye Qin[1†], Zijin Yang[1†], Po-Sheng Huang[2†], Xinyang Mu[1†], Shih-Hsiu Huang[2], Yuzhi Shi[3*], Wannian Zhao[1], Bo Li[1,4], Ji Zhou[5], Jesús Zúñiga-Pérez[6,7,8], Patrice Genevet[6,9*], Pin Chieh Wu[2,10,11*], Qinghua Song[1,4*]

[1] Institute of Materials Research (IMR), Tsinghua Shenzhen International Graduate School, Tsinghua University, Shenzhen, 518055, China

[2] Department of Photonics, National Cheng Kung University, Tainan 70101, Taiwan, Republic of China

[3] Institute of Precision Optical Engineering, School of Physics Science and Engineering, Tongji University, Shanghai 200092, China

[4] Suzhou Laboratory, Suzhou 215000, China

[5] State Key Laboratory of New Ceramics and Fine Processing, School of Materials Science and Engineering, Tsinghua University, Beijing 100084, China

[6] Université Côte d'Azur, CNRS, Centre de Recherche sur l'Hétéro-Epitaxie et ses Applications, Rue Bernard Gregory, Sophia Antipolis, 06560 Valbonne, France

[7] MajuLab, International Research Laboratory IRL 3654, CNRS, Université Côte d'Azur, Sorbonne Université, National University of Singapore, Nanyang Technological University, Singapore, Singapore

[8] Division of Physics and Applied Physics, School of Physical and Mathematical Sciences, Nanyang Technological University, Singapore 637371, Singapore

[9] Physics department, Colorado School of Mines, 1523 Illinois Street, Golden, CO 80401, US

[10] Center for Quantum Frontiers of Research & Technology (QFort), National Cheng Kung University, Tainan, 70101, Taiwan, Republic of China

[11] Meta-nanoPhotonics Center, National Cheng Kung University, Tainan, 70101, Taiwan, Republic of China

[†]These authors contributed equally to this work.

*Corresponding authors: yzshi@tongji.edu.cn; Patrice.Genevet@mines.edu; pcwu@gs.ncku.edu.tw; song.qinghua@sz.tsinghua.edu.cn;

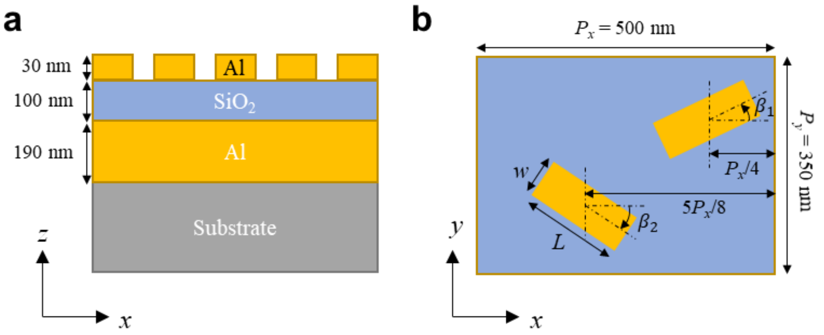

Fig. S1. Structure design of the metasurface. a Side view of the metasurface, which consists of a metal-dielectric-metal layers stack fabricated on a silicon substrate. The bottom metallic layer blocks all the transmission, such that the metasurface works in reflective regime. **b** Top view of one unit cell of the metasurface. Two metal nanorods serve as two decoupled scatterers with individually tunable rotation angles (β_1, β_2).

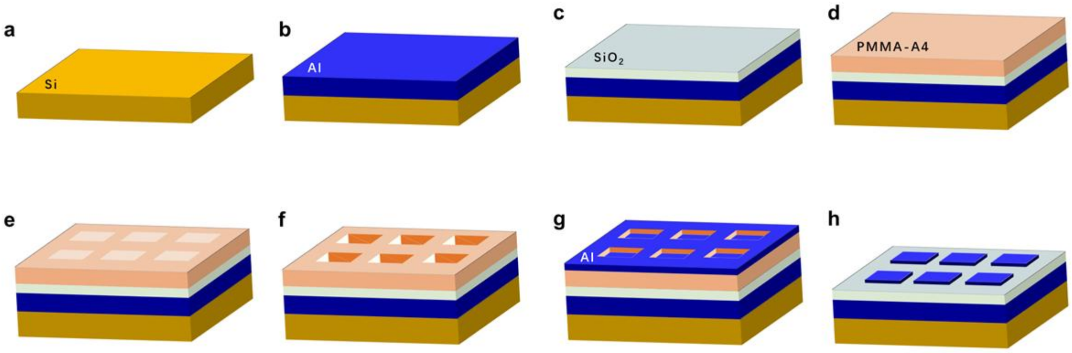

Fig. S2. Fabrication process of plasmonic non-Hermitian metasurfaces. a The cleaned silicon wafer is cut into 1 × 1 cm^2 square substrates. **b** A 150 nm thick aluminum (Al) layer is then deposited on the substrate using thermal evaporation to serve as the ground layer. **c** A 40 nm SiO_2 spacer layer is applied onto the Al layer via magnetron sputtering. **d** A ~120 nm thick layer of CSAR 62 resist is spin-coated onto the spacer. **e** E-beam lithography is used for pattern exposure at 50 kV. **f** Development in ZED-N50 for 4.5 minutes. **g** A 30 nm Al layer is then deposited using thermal evaporation. **h** Lift-off process in Remover-PG, followed by rinsing in IPA and deionized water.

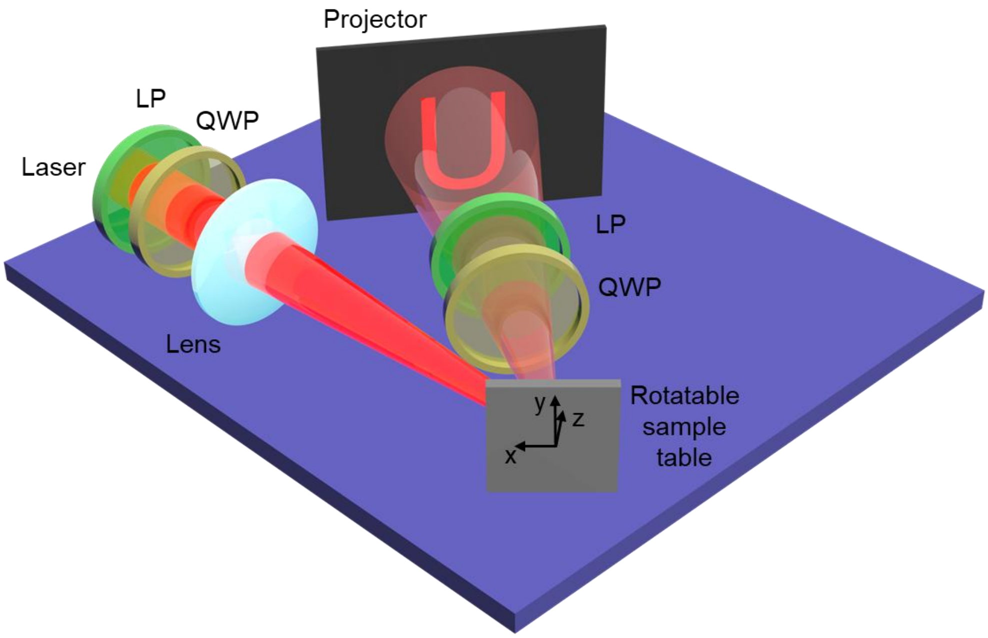

Fig. S3. Optical setup for the measurement of meta-holograms. A laser beam with a set wavelength propagates through a linear polarizer (LP) and a quarter-wave plate (QWP) to obtain a beam in a specific polarization state. Then the laser beam passes through the lens and is weakly focused on the metasurface, which is fixed on a rotatable sample table. The sample table can rotate independently along the *z*-axis and *y*-axis to realize the adjustment of azimuth (α) and altitude angle (θ). A projector is placed in the direction of the -1st order diffraction to record the meta-hologram. In the direction of the diffracted light another set of quarter-wave plate and linear polarizer is placed between the projector and the metasurface, so that the beam with orthogonal polarization to the incident light can pass through, and the reflected hologram is projected onto the projector.

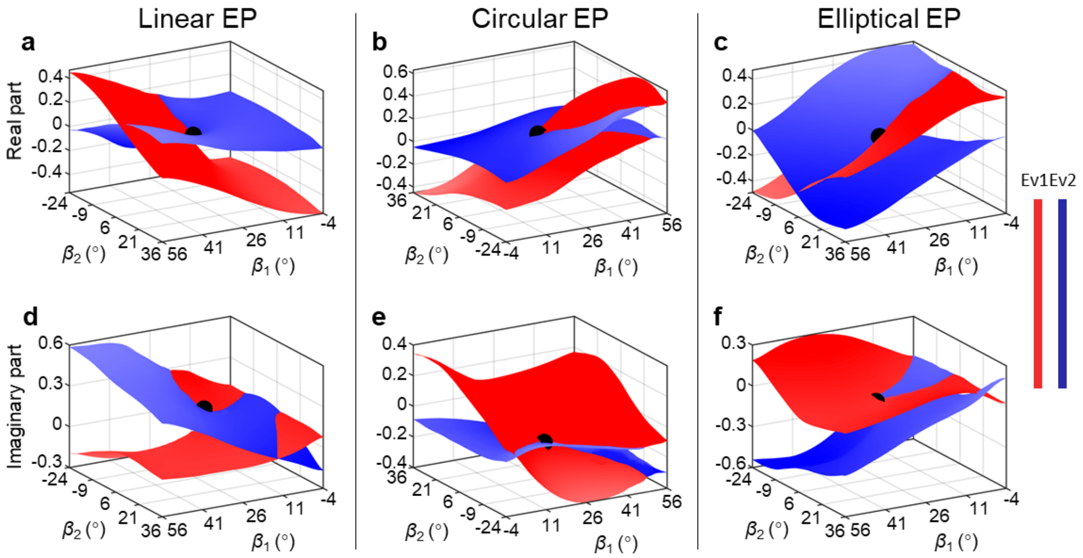

Fig. S4. Exceptional points in the two-dimensional parameter space (β_1, β_2), for degenerate eigenstates displaying linear (first column), circular (second column), and elliptical polarization (third column). Real (**a-c**) and imaginary (**d-f**) parts of the eigenvalues of the simulated reflection matrix J around arbitrary EP in the parameter space of the nanorod rotation angles (β_1, β_2). The EPs occur at the same rotation angles $(\beta_1, \beta_2) = (26°, 6°)$, represented as black dots. At the three EPs, both real and imaginary parts of the eigenvalues coalesce. The corresponding incident conditions (α, θ) for the three columns are $(0°, 60°)$, $(31°, 67°)$ and $(15°, 70°)$, respectively.

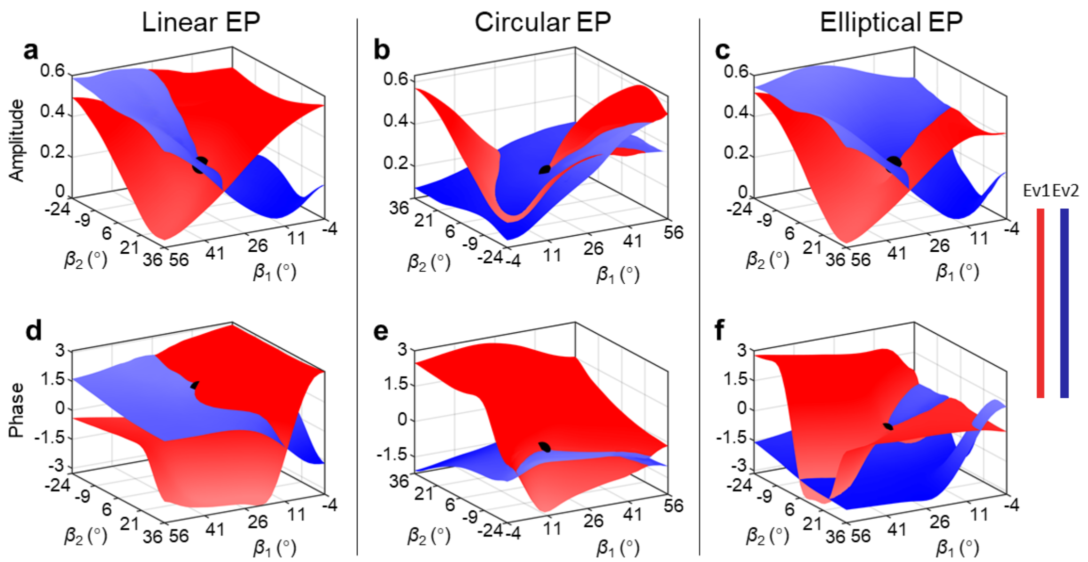

Fig. S5. Exceptional points in the two-dimensional parameter space (β_1, β_2), for degenerate eigenstates displaying linear (first column), circular (second column), and elliptical polarization (third column). Amplitude (**a-c**) and phase (**d-f**) of the eigenvalues of the simulated reflection matrix J around arbitrary EP in the parameter space of the nanorod rotation angles (β_1, β_2). The EPs occur at the same rotation angles $(\beta_1, \beta_2) = (26°, 6°)$, represented as black dots. At the three EPs, both real and imaginary parts of the eigenvalues coalesce. The corresponding incident conditions (α, θ) for the three columns are $(0°, 60°)$, $(31°, 67°)$ and $(15°, 70°)$, respectively.

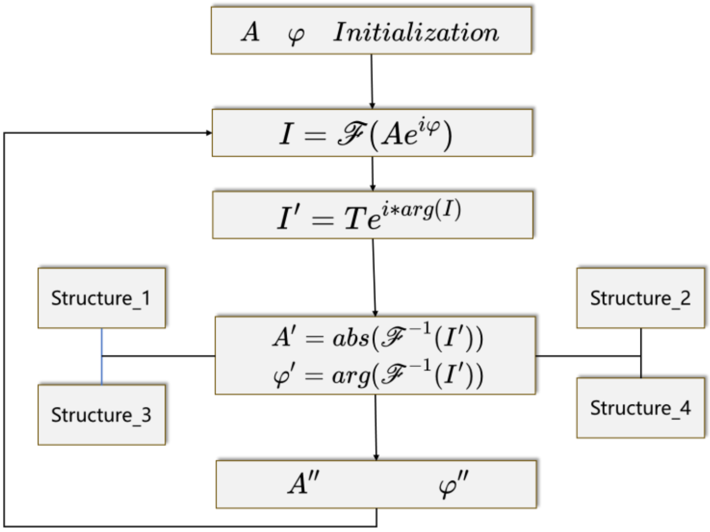

Fig. S6 Flowchart for the holographic optimization algorithm. First, random amplitude and phase (A and φ) are used as the initial dataset for calculation. Subsequently, the far-field holograms (I) are obtained by performing Fourier transform on linear, circular, and elliptical polarization channels respectively. The amplitude is replaced by a corresponding target image (T), and the phase and amplitude of different channels are updated by inverse Fourier transform. To accommodate for structural constraints, these phases and amplitude (A' and φ') are matched to four topological phase-delaying elements by Euclidean distance. After matching, the updated phase and amplitude (A'' and φ'') continue to be optimized iteratively. In the end, the spatial phase distribution is validated after convergence.

Supplementary Note S1: Dipole model for reflection matrix

Assuming that the two nanorods in each period of the plasmonic metasurface have dipole moments polarized along the direction of their arms, the dipole moments ($\boldsymbol{E}_{1,2}$) can be obtained by decomposing incident light ($\boldsymbol{E}_{ix,iy}$) along the directions of nanorods

$$\boldsymbol{E}_1 = C\left(\boldsymbol{E}_{ix}\, cos\, \beta_1\, e^{i\delta_1} + \boldsymbol{E}_{iy}\, cos\, \beta_1\, e^{i\delta_1}\right) \tag{1}$$

$$\boldsymbol{E}_2 = C\left(\boldsymbol{E}_{ix}\, cos\, \beta_2\, e^{i\delta_2} + \boldsymbol{E}_{iy}\, cos\, \beta_2\, e^{i\delta_2}\right) \tag{2}$$

By superposition of the dipole moments in *xy* direction, the output light ($\mathbf{E}_{ox,oy}$) reads

$$\boldsymbol{E}_{ox} = \boldsymbol{E}_{1x} + \boldsymbol{E}_{2x} \tag{3}$$

$$\boldsymbol{E}_{oy} = \boldsymbol{E}_{1y} + \boldsymbol{E}_{2y} \tag{4}$$

The reflection matrix J_0 connecting $\left[\boldsymbol{E}_{ix}, \boldsymbol{E}_{iy}\right]^T$ and $\left[\boldsymbol{E}_{ox}, \boldsymbol{E}_{oy}\right]^T$ can be obtained under global *xoy* coordinates[1,2]

$$J_0 = C\begin{pmatrix} \cos^2\beta_1 e^{i\delta_1} + \cos^2\beta_2 e^{i\delta_2} & \sin\beta_1\, cos\,\beta_1 e^{i\delta_1} + \sin\beta_2\, cos\,\beta_2 e^{i\delta_2} \\ \sin\beta_1\, cos\,\beta_1 e^{i\delta_1} + \sin\beta_2\, cos\,\beta_2 e^{i\delta_2} & \sin^2\beta_1 e^{i\delta_1} + \sin^2\beta_2 e^{i\delta_2} \end{pmatrix} \tag{5}$$

where $\delta_{1,2}$ are the detour phases induced by displacement of two nanorods, *C* is a complex valued constant. To convert the reflection matrix J_0 to matrix J_{obl} under oblique incidence, with local orthogonal $\{\mathbf{s}, \mathbf{p}, \mathbf{k}\}$ basis propagating along with wave vector $\mathbf{k}$, the three-dimensional orthogonal transformation is introduced[3], which gives

$$J_{obl} = O_{out,q}^{-1} J_0 O_{in,q} \tag{6}$$

where J_0 is expanded to 3×3 by omitting z component and the transformation matrices are given as

$$O_{in,q}^{-1} = \begin{pmatrix} s_{x,q} & s_{y,q} & s_{z,q} \\ p_{x,q} & p_{y,q} & p_{z,q} \\ k_{x,q-1} & k_{y,q-1} & k_{z,q-1} \end{pmatrix} \tag{7}$$

$$O_{out,q} = \begin{pmatrix} s_{x,q} & p'_{x,q} & k_{x,q} \\ s_{y,q} & p'_{y,q} & k_{z,q} \\ s_{z,q} & p'_{z,q} & k_{z,q} \end{pmatrix} \tag{8}$$

where $\boldsymbol{s}_q = \frac{\boldsymbol{k}_{q-1} \times \boldsymbol{k}_q}{|\boldsymbol{k}_{q-1} \times \boldsymbol{k}_q|}$, $\boldsymbol{p}_q = \boldsymbol{k}_{q-1} \times \boldsymbol{s}_q$, $\boldsymbol{s}'_q = \boldsymbol{s}_q$, and $\boldsymbol{p}'_q = \boldsymbol{k}_q \times \boldsymbol{s}_q$. All vectors are normalized to unit length.

The incident wave vector is $\boldsymbol{k}_{q-1} = (-sin(\theta), 0, -cos(\theta))$ with θ being the incident angle. By employing the diffraction equation, the -1st diffraction angle reads

$$\theta_d = \arcsin\left[\frac{\lambda}{p_0} - sin\,(\theta)\right] \tag{9}$$

Leading to the diffraction wave vector $\boldsymbol{k}_q = (sin(\theta_d), 0, cos(\theta_d))$.

With the above-mentioned formalism, diffraction reflection matrix J_{obl} with local $\{\boldsymbol{s}, \boldsymbol{p}\}$ basis can be calculated. Since we focus on polarization responses, we omit the electric component in z direction in J_{obl}.

Supplementary Note S2: Deviation of diffraction wave vector in three-dimensional diffraction

In the general case, the diffraction vector is not necessarily contained in the plane defined by the incident vector and the vector normal to the metasurface, resulting in a three-dimensional diffraction. This can happen when we tune the incident azimuth angle α away from zero.

The wave vector for Floquet periodicity is $\boldsymbol{k}_F = |\boldsymbol{k}| sin\,(\theta)[\boldsymbol{a}_1\, cos(\alpha) + \boldsymbol{n} \times \boldsymbol{a}_1 sin\,(\alpha)]$, where $\boldsymbol{a}_{1,2}$ is the primitive unit cell vector, and $\boldsymbol{n} = \frac{\boldsymbol{a}_1 \times \boldsymbol{a}_2}{|\boldsymbol{a}_1 \times \boldsymbol{a}_2|}$ is the normal vector. The reciprocal lattice vectors are described as:

$$\boldsymbol{G}_1 = 2\pi \frac{\boldsymbol{a}_2 \times \boldsymbol{n}}{\boldsymbol{a}_1 \boldsymbol{a}_2 \times \boldsymbol{n}}, \boldsymbol{G}_2 = 2\pi \frac{\boldsymbol{n} \times \boldsymbol{a}_1}{\boldsymbol{a}_1 \boldsymbol{a}_2 \times \boldsymbol{n}} \tag{10}$$

The diffraction wave vector is calculated separately for the parallel and perpendicular component of the metasurface plane,

$$\boldsymbol{k}_{diff,\parallel} = \boldsymbol{k}_F + M\boldsymbol{G}_1 + N\boldsymbol{G}_2 \tag{11}$$

$$\boldsymbol{k}_{diff,\perp} = \boldsymbol{n}\sqrt{\boldsymbol{k}^2 - \boldsymbol{k}_{diff,\parallel}^2} \tag{12}$$

With *M*, *N* denoting the diffraction order. Therefore, the three-dimensional diffraction vector can be expressed as

$$\boldsymbol{k}_{diff} = \boldsymbol{k}_{diff,\parallel} + \boldsymbol{k}_{diff,\perp} \tag{13}$$

With the calculated diffraction vector and incident vector, we can obtain the diffraction reflection matrix under various bases. In particular, the diffraction reflection matrix under oblique incidence in ($\boldsymbol{s}$, $\boldsymbol{p}$) polarization basis can be calculated as,

$$J_{obl} = \begin{pmatrix} J_{ss} & J_{sp} \\ J_{ps} & J_{pp} \end{pmatrix} = [O_{out}^{-1} J_0 O_{in}]_{2\times 2} \tag{14}$$

where $[M]_{2\times 2}$ is the operator taking the first 2-by-2 submatrix of *M*. The comparison of the simulated results of J_{ps} terms in the diffraction reflection matrix from the dipole model and the FEM simulation method are shown in Fig. S7. The position of the four zeros matches very well.

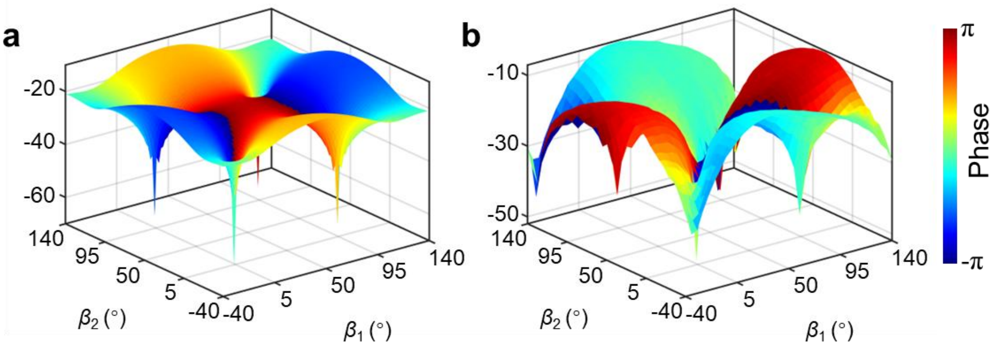

Fig. S7 Comparison of the simulated result of J_{sp} terms in diffraction reflection matrix obtained from (a) dipole model and (b) FEM method. Since the dipole model fails to include the size and coupling between nanorods, there exists some deviation between the two results. However, the positions of the four zeros match very well.

Supplementary Note S3: EP under symmetric and asymmetric basis change

For a specific Jones matrix J under linear polarization basis (measured under xy or sp polarization basis), B is an arbitrary invertible matrix that can lead to basis transformation through:

$$J' = B^{-1}JB \tag{15}$$

We assume eigenvalues and eigenstates of J are $\lambda_{1,2}$ and $\mathbf{v}_{1,2}$. For EP the condition reads $\lambda_1 = \lambda_2 = \lambda$ and $\boldsymbol{v}_1 = \boldsymbol{v}_2 = \boldsymbol{v}$. When J is at EP, it can be easily proved that this kind of "symmetric" basis change does not break EP condition for J', but it transforms the eigenstate to $B^{-1}\mathbf{v}$. While for asymmetric basis change with $B_1 \neq B_2$,

$$J'' = B_1^{-1}JB_2 \tag{16}$$

the eigenvalues of J and J'' are not the same. B_1 and B_2 can be defined by choosing four different polarization states ($\boldsymbol{p}_1, \boldsymbol{p}_2, \boldsymbol{p}_3, \boldsymbol{p}_4$) on the Poincaré sphere, for example, as

$$B_1 = [\boldsymbol{p}_1; \boldsymbol{p}_2], B_2 = [\boldsymbol{p}_3; \boldsymbol{p}_4] \tag{17}$$

For a 2D achiral system, the Jones matrix can be generally written as

$$J = \begin{pmatrix} a & b \\ b & d \end{pmatrix} \tag{18}$$

with identical anti-diagonal components. This kind of constraint fixes EP eigenstates to be circularly polarized $[1, \pm i]^T$. Then the EP topological phase reveals under the orthogonal basis (EP eigenstate and its orthogonal, that is, two eigenstates with circular polarization) by employing symmetric basis change with $B = [(1, i)^T; (1, -i)^T]$.

Therefore, for 2D achiral system, EP and EP associated topological phase can only emerge under circular polarization.

In order to realize EP and EP associated topological phase at other polarization states (elliptical and linear polarized states), chirality is required, which introduces a new degree of freedom in the Jones matrix,

$$J = \begin{pmatrix} a & b \\ c & d \end{pmatrix} \tag{19}$$

leading to non-identical anti-diagonal components. This chirality-induced new degree of freedom relieves the constraint of circular-polarized eigenstates, having a more general EP eigenstate with

$$\boldsymbol{v} = \left[\sqrt{b}, \pm i\sqrt{c}\right]^T \tag{20}$$

which can be readily engineered to become linearly, circularly, or even elliptically polarized.

Supplementary Note S4: Asymmetric basis transformation based on the EP eigenstates and its orthogonal counterpart

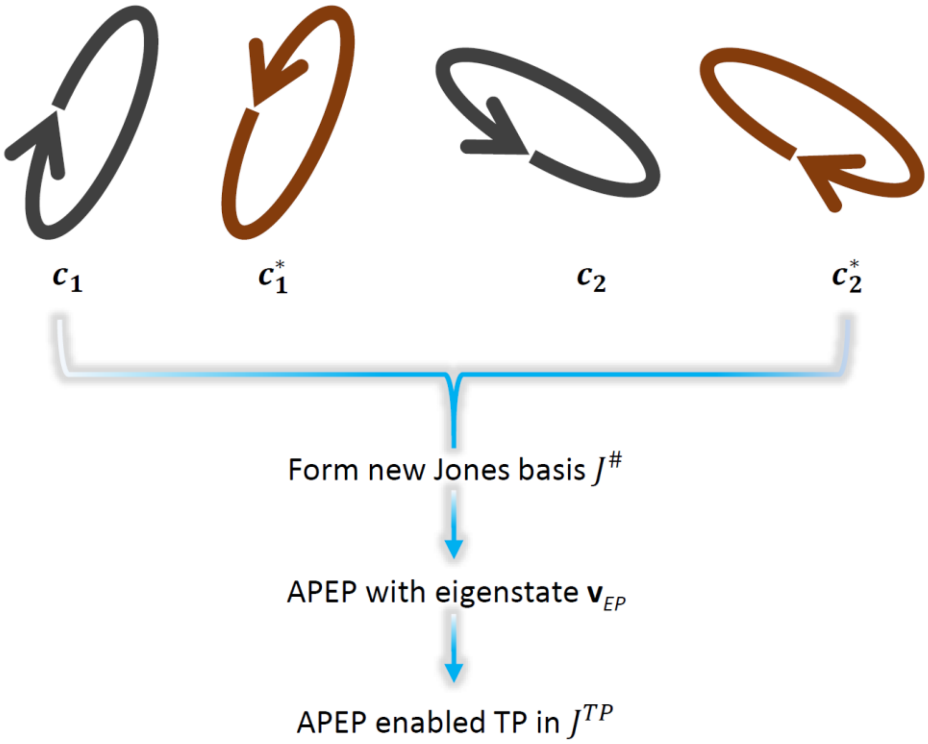

Fig. S8. Relationship of the polarization basis and the calculation flow for obtaining the reflection matrix.

The reflection matrix describing the -1st order diffraction and polarization conversion for the plasmonic metasurface can be directly obtained under local $\{\boldsymbol{s},\boldsymbol{p}\}$ basis as

$$J_{obl}=\begin{pmatrix} J_{ss} & J_{sp} \\ J_{ps} & J_{pp} \end{pmatrix} \tag{21}$$

where $\{\boldsymbol{s},\boldsymbol{p}\}$ is the in-plane and out-of-plane polarization vector, respectively, and the reference plane is defined by the propagation wavevector $\mathbf{k}$ and vector normal to the metasurface plane. The matrix elements J_{mn} represent the conversion coefficients from polarization state n to state m. The input and output vectors then are $\mathbf{i}^{sp}=(i_s,i_p)$ and $\mathbf{o}^{sp}=(o_s,o_p)$.

To evaluate the proposed arbitrary exceptional point, we change from the $\{\boldsymbol{s},\boldsymbol{p}\}$ basis to the $\{c_1,c_2\}_{in},\{c_1^*,c_2^*\}_{out}$ for the input and output orthogonal basis, where $c_j^*\ \{j=1,2\}$ denotes the counter-clockwise rotating polarization state of $c_j\ \{j=1,2\}$. The redefined reflection matrix can be written as

$$J^{\#} = \begin{pmatrix} J_{c_1^* c_1} & J_{c_1^* c_2} \\ J_{c_2^* c_1} & J_{c_2^* c_2} \end{pmatrix} \tag{22}$$

The corresponding input and output vectors are $\boldsymbol{i}^{c_1 c_2} = (i_{c_1}, i_{c_2})$ and $\boldsymbol{o}^{c_1^* c_2^*} = (o_{c_1^*}, o_{c_2^*})$.

The conversion matrix that connects different bases is given by

$$\boldsymbol{i}^{sp} = \Gamma_i = [c_1\ c_2] * \boldsymbol{i}^{c_1 c_2}, \boldsymbol{o}^{sp} = \Gamma_o = [c_1^*\ c_2^*] * \boldsymbol{o}^{c_1^* c_2^*} \tag{23}$$

where $\{c_1, c_2\}_{in}, \{c_1^*, c_2^*\}_{out}$ constitute orthogonal bases, and $\Gamma_{\mathrm{i,o}}$ is the transformation which will maintain the EP condition for symmetric transformation like $\Gamma_i^{-1} J \Gamma_i$ and $\Gamma_o^{-1} J \Gamma_o$. The redefined reflection matrix $J^{\#}$ undergoes asymmetric transformation, since

$$J^{\#} = \Gamma_{\mathrm{o}}^{-1} J \Gamma_{\mathrm{i}} \tag{24}$$

which is employed to realize EP under different bases $\{c_1, c_2\}_{in}, \{c_1^*, c_2^*\}_{out}$. Assume the eigenvalues and eigenstates of $J^{\#}$ are $\lambda_{1,2}$ and $\{\boldsymbol{v}_{1,2}\}$, at EP, $\lambda_1 = \lambda_2$ and $\boldsymbol{v}_1 = \boldsymbol{v}_2 = \boldsymbol{v}_{EP}$. To reveal the topological phase under arbitrary EP, the state orthogonal to $\boldsymbol{v}_{EP}$ is defined as $\boldsymbol{v}_{EP}^{O}$, thus forming a new orthogonal basis of $(\boldsymbol{v}_{EP}, \boldsymbol{v}_{EP}^{O})$ under $\{c_1, c_2\}_{in}, \{c_1^*, c_2^*\}_{out}$ bases.

Such asymmetric basis transformation provides an infinitely continuous search space (corresponding to the whole surface of Poincaré sphere) for finding fine-tuned arbitrary EPs that require exactly coalesced eigenvalues. With a specific Jones matrix J_{obl} in a fixed sample and determined incidence conditions (α, θ), we conduct parameter sweep by varying the arbitrary orthogonal polarization pairs $\{c_1, c_2\}$ and $\{c_1^*, c_2^*\}$ through the surface of Poincaré sphere to find exact EP position in Jones matrix $J^{\#}$. When an arbitrary EP is found, the asymmetric basis transformation $(\{c_1, c_2\}_{in}, \{c_1^*, c_2^*\}_{out})$ is settled, with fixed $J^{\#}$, and EP induced singularity and topological phase is retrieved through a symmetric transformation as follows (denoted as J^{TP}), which does not impact the eigenvalues (Fig. S8).

At the EP condition of $J^{\#}$, we perform the symmetric transformation $\Gamma_{EP} = [\boldsymbol{v}_{EP}\ \boldsymbol{v}_{EP}^{O}]$ not impacting EP (as proved in Supplementary Note S3)

$$J^{TP} = \Gamma_{EP}^{-1} J^{\#} \Gamma_{EP} \tag{25}$$

where J^{TP} is the reflection matrix manifesting zero singularity and thus topological phase in parameter space on its anti-diagonal term. It is important to note that although $\boldsymbol{v}_{EP}$ and $\boldsymbol{v}_{EP}^{O}$ are orthogonal for Jones matrix $J^{\#}$ under asymmetric bases $\{c_1, c_2\}_{in}, \{c_1^*, c_2^*\}_{out}$, they are not orthogonal under $\{\boldsymbol{s}, \boldsymbol{p}\}$ basis. The sequential asymmetric-symmetric basis transformation can be denoted as $\{\boldsymbol{s}, \boldsymbol{p}\} \rightarrow \{TP\}$. Generally, J^{TP} will have decoupled anti-diagonal terms in the demanded form for arbitrary EP

$$J^{TP} = \begin{pmatrix} a & b \\ c & d \end{pmatrix} \rightarrow J \tag{26}$$

and we simplify its notation to J in the main text for concision. The diagonal terms of matrix J are referred to as $J_{1,1}$ and $J_{2,2}$, and the anti-diagonal term as $J_{1,2}$ and $J_{2,1}$. In the main text, the Jones matrix element $J_{i,j}$ in Figs. 2-5 represents polarization conversion. For the linear EP, $J_{1,2}$ represents the polarization state conversion from $(\chi, \phi) = (0°, -30°)$ to $(14°, -66°)$. For the circular EP, $J_{1,2}$ represents the polarization state conversion from $(\chi, \phi) = (45°, 0°)$ to $(22°, 23°)$. For the elliptical EP, it's the polarization state conversion from $(\chi, \phi) = (18°, -53°)$ to $(16°, -15°)$.

The input and output states are obtained by cascaded transformation

$$\boldsymbol{i}^{sp} = \Gamma_i \Gamma_{EP} \boldsymbol{i}^{TP}, \quad \boldsymbol{o}^{sp} = \Gamma_o \Gamma_{EP} \boldsymbol{o}^{TP} \tag{27}$$

It is noted that $\boldsymbol{v}_{EP}$ happens under the $\{c_1, c_2\}_{in}, \{c_1^*, c_2^*\}_{out}$ bases, therefore the EP state under local $\{\boldsymbol{s}, \boldsymbol{p}\}$ basis is given by $\boldsymbol{i}_{EP}^{sp} = [c_1\ c_2]\boldsymbol{v}_{EP}$, $\boldsymbol{o}_{EP}^{sp} = [c_1^*\ c_2^*]\boldsymbol{v}_{EP}$, and similarly for $\boldsymbol{v}_{EP}^{O}$ as $\boldsymbol{i}_{EP^O}^{sp} = [c_1\ c_2]\boldsymbol{v}_{EP}^{O}$, $\boldsymbol{o}_{EP^O}^{sp} = [c_1^*\ c_2^*]\boldsymbol{v}_{EP}^{O}$. The topological phase can be retrieved with the incident state $\boldsymbol{i}_{EP}^{sp}$ and output detection state $\boldsymbol{o}_{EP^O}^{sp}$. The process of employing EP to retrieve topological phase is illustrated in Fig. S9.

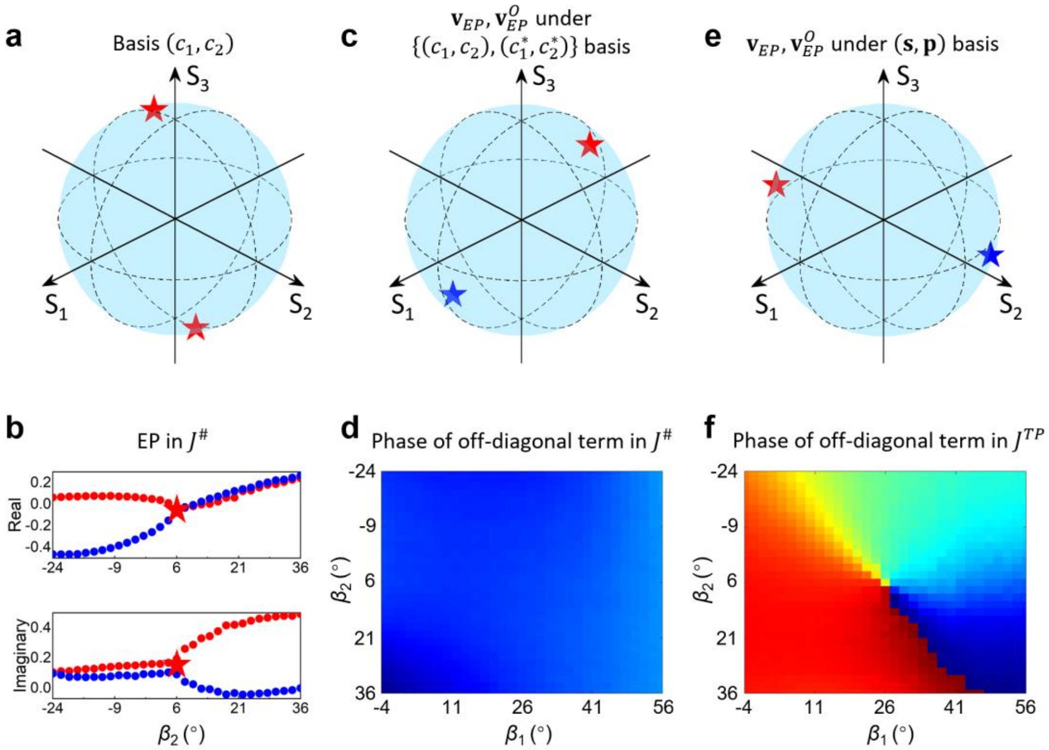

Fig. S9. Demonstration of EP in reflection matrix and retrieved EP topological phase. a The EP is first found by changing basis of $J^{\#}$. When the EP condition is fulfilled, the basis is set to (c_1, c_2), plotted under global basis. **b** Eigenstates of EP, and its orthogonality on Poincaré sphere under basis of $J^{\#}$. **c** $J^{\#}$ is then transformed with $\Gamma_{EP} = [\boldsymbol{v}_{EP}\ \boldsymbol{v}_{EP}^{O}]$ to J^{TP}. The process maintains EP condition in **b**. **d** Real and imaginary part of eigenvalues of transformed Jones matrix $J^{\#}$. EP happens around $\beta_2 = 6°$. **e** Topological phase does not reveal on anti-diagonal term in $J^{\#}$. **f** Topological phase is retrieved in J^{TP} by transforming Jones matrix to reveal singularity.

Supplementary Note S5: Arbitrarily polarized topological phase under different incident conditions with a fixed structure

For a fixed structure, arbitrarily polarized topological phase can be realized under different incident conditions. Taking the structure $(\beta_1, \beta_2) = (26°, 6°)$ as an example, we illustrate four EP polarization states in Fig. S10 with two anti-diagonal terms in Jones matrix J_{obl} and J^{TP}. EPs with topological phase in J^{TP} showing linear polarization (Fig. S10a), elliptical polarization (Fig. S10b and S10c), and circular polarization (Fig. S10d) are demonstrated in a fixed structure by only modifying the incident conditions.

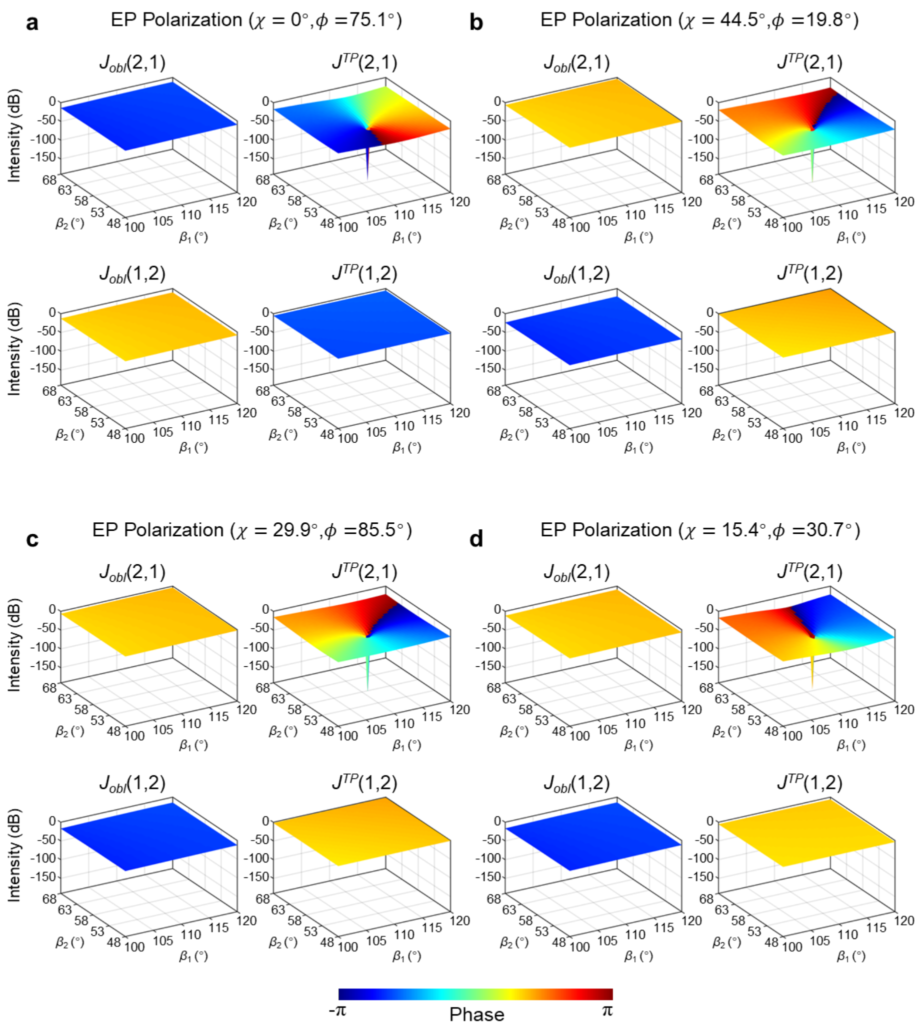

Fig. S10. Arbitrarily polarized topological phase under different incident conditions with a fixed structure. a Linear polarization. **b** and **c** Elliptical polarization. **d** Circular polarization.

Supplementary Note S6: Extension of EP with arbitrarily polarized eigenstates from optical systems described by Jones matrix to Hamiltonian

Although we explore exceptional points in Jones matrices, which describe the polarization conversion of optical systems, breaking the degeneracy of anti-diagonal terms may also be possible in systems described by a Hamiltonian through the introduction of asymmetric coupling.

In the most common case of a 2×2 Hamiltonian,

$$H = \begin{bmatrix} \omega_1 - i\gamma_1 & \kappa \\ \kappa & \omega_2 - i\gamma_2 \end{bmatrix} \tag{28}$$

with symmetric coupling strength on the diagonal term[4], it is easily proved that the eigenstate at the EP corresponds to a circular one with $\boldsymbol{v}_{EP} = (1, \pm i)^T$.

Asymmetric coupling can be made possible with nonlinearity, magnetic field, and/or time modulation[5-7]. Here, we demonstrate the appearance of EP eigenstates under symmetric coupling, asymmetric coupling with external phase and unequal amplitude. Their 2×2 Hamiltonians read

$$H_1 = \begin{bmatrix} \omega_1 - i\gamma_1 & \kappa e^{i\psi} \\ \kappa & \omega_2 - i\gamma_2 \end{bmatrix} \tag{29}$$

$$H_2 = \begin{bmatrix} \omega_1 - i\gamma_1 & \kappa_1 \\ \kappa_2 & \omega_2 - i\gamma_2 \end{bmatrix} \tag{30}$$

$$H_3 = \begin{bmatrix} \omega_1 - i\gamma_1 & \kappa_1 e^{i\psi_1} \\ \kappa_2 e^{i\psi_2} & \omega_2 - i\gamma_2 \end{bmatrix} \tag{31}$$

where $\psi, \kappa_{1,2} \in \Re$.

The EP eigenstates on the Poincaré sphere without and with asymmetric coupling are shown in Fig. S11. When coupling is symmetric, the degenerate eigenstate is circularly polarized, as expected in Fig. S11a. Introduction of asymmetry in phase, amplitude, or both in the coupling terms for Hamiltonians $H_{1,2,3}$ results in a deviation from circular states in Fig. S11b-d, respectively. Therefore, our proposed arbitrary EP may also play a decisive role in Hamiltonian system with asymmetric coupling, which could contribute to chiral mode conversion, EP sensing, dynamics, and topology.

For example, encircling EP in anti-PT-symmetric system leads to chiral dynamics or non-chiral dynamics depending on the starting point[8]. Upon encircling, the two eigenvectors are solved to be $|\boldsymbol{\psi}_A\rangle = \left[1, i\left(\rho + 1 + \sqrt{\rho^2 + 2\rho}\right)\right]^T$ and $|\boldsymbol{\psi}_B\rangle =$

$\left[1, i\left(\rho + 1 - \sqrt{\rho^2 + 2\rho}\right)\right]^T$, where ρ is the loop radius. EP happens at the center of the encircling loop with $\rho = 0$ and circular eigenstate, which limits the coverage of loop eigenstates. By the introduction of asymmetric coupling, EP eigenstate can become arbitrary, and eigenstates of encircling loops will cover more region on Poincaré sphere. This indicates a more versatile mode conversion among coupled waveguides for different phases rather than only symmetric (0) and anti-symmetric ($\pi/2$) one.

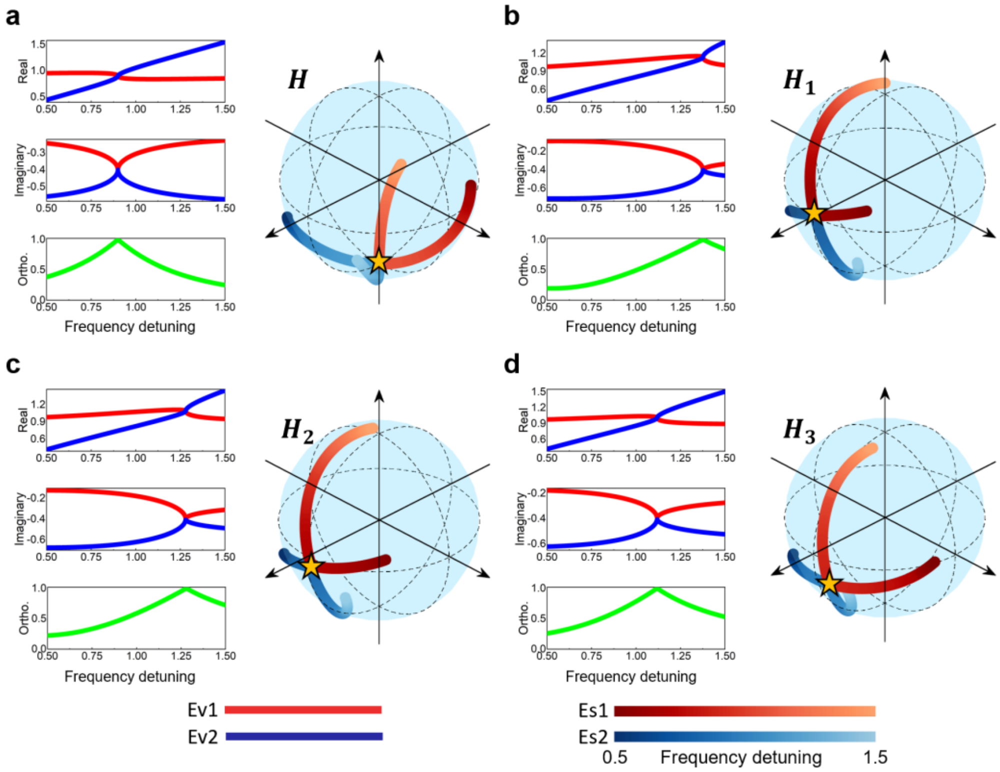

Fig. S11. Arbitrary EP eigenstate for Hamiltonian systems. Real and imaginary parts of eigenvalues of Hamiltonians and the orthogonality of eigenstates for **a** symmetric coupling with circular eigenstate; **b-d** asymmetric coupling with non-circular degeneracy. The evolution of eigenstates is illustrated on Poincaré sphere. Unit orthogonality indicates that the two eigenstates coalesced.

Supplementary Note S7: Universality of the concept of EP with arbitrary polarization eigenstates

It is worth noting that the proposed idea of generating arbitrary EP and using them to control the polarization of light beams can be applied to a wide range of EP systems, including those described by Hamiltonian and scattering matrices, hereafter referred to as Hamiltonian system and scattering system. To demonstrate the universality of the concept of arbitrary EP, we apply it to several different EP systems, including Hamiltonian and scattering systems[4,8-15]. Two of these examples are analyzed in detail:

(1) **Arbitrary EPs in the Hamiltonian system**. From the perspective of two modes ($|a\rangle$, $|d\rangle$) with coupling strength of b, c, conventional EP features a circular eigenstate of $(1, \pm i)^T$, implying that at EP the system will degenerate to the coalesced eigenstate which is a superposition of two decoupled eigenmodes. However, this comes at the cost of a fixed $\pi/2$ phase difference and equal amplitudes[1,2]. In contrast, arbitrary EP offers a broader range of possibilities, allowing for superpositions with arbitrary phase and amplitude between two eigenmodes, thus contributing to more diverse EP eigenstates. Consider a scenario where $|a\rangle = cw, |d\rangle = ccw$, where cw, ccw correspond to clockwise and counterclockwise propagating modes (for example, whispering gallery modes in ring resonators). The degenerated arbitrary EP eigenstate is $\sqrt{b}\,|a\rangle + e^{\pm j\pi/2}\sqrt{c}|d\rangle$ that shows arbitrary superposition of two modes $|a\rangle, |d\rangle$ in phase and amplitude, in sharp contrast to conventional EP eigenstate of $|a\rangle + e^{\pm j\pi/2}|d\rangle$. As for arbitrary EP, if $b \neq c$ and setting $c = 0$, we obtain an EP where only the cw mode exists. Meanwhile, conventional EP cannot be made possible since it processes both modes of equal amplitude. This can be employed for modulating chirality and enabling chiral lasing action at EP, allowing us to intentionally choose a specific chiral mode to prevail at EP.

(2) **Arbitrary EPs in the scattering system**. Another application of our strategy consists in expanding coherent perfect absorption (CPA) at EP to arbitrary eigenstates in scattering systems with arbitrary phase-amplitude combination. CPA at EP has been proposed and realized as an intriguing phenomenon with broaden absorption spectrum and distinct scattering properties. However, currently CPA at EP is only limited to circularly-polarized eigenstates, indicating the two injections at port 1 and port 2 need to be perfectly aligned, with equal amplitude and $\pi/2$ phase delay[12]. While arbitrary EP will greatly widen the applicable conditions for practical usage with any combination of amplitude ratio and phase retardation, thus unfolding the unexplored distinct spectral singularities.

Supplementary Note S8: Robustness of EP against structural disorder and fabrication imperfections

First, we introduce a fillet to the sharp corner of the metal nanorod in Fig. S12. Introduction and increase of fillet radius of the nanorods have no impact on the existence of EP, while slightly shifting the occurrence of EP in wavelength and eigenpolarization state on Poincaré sphere.

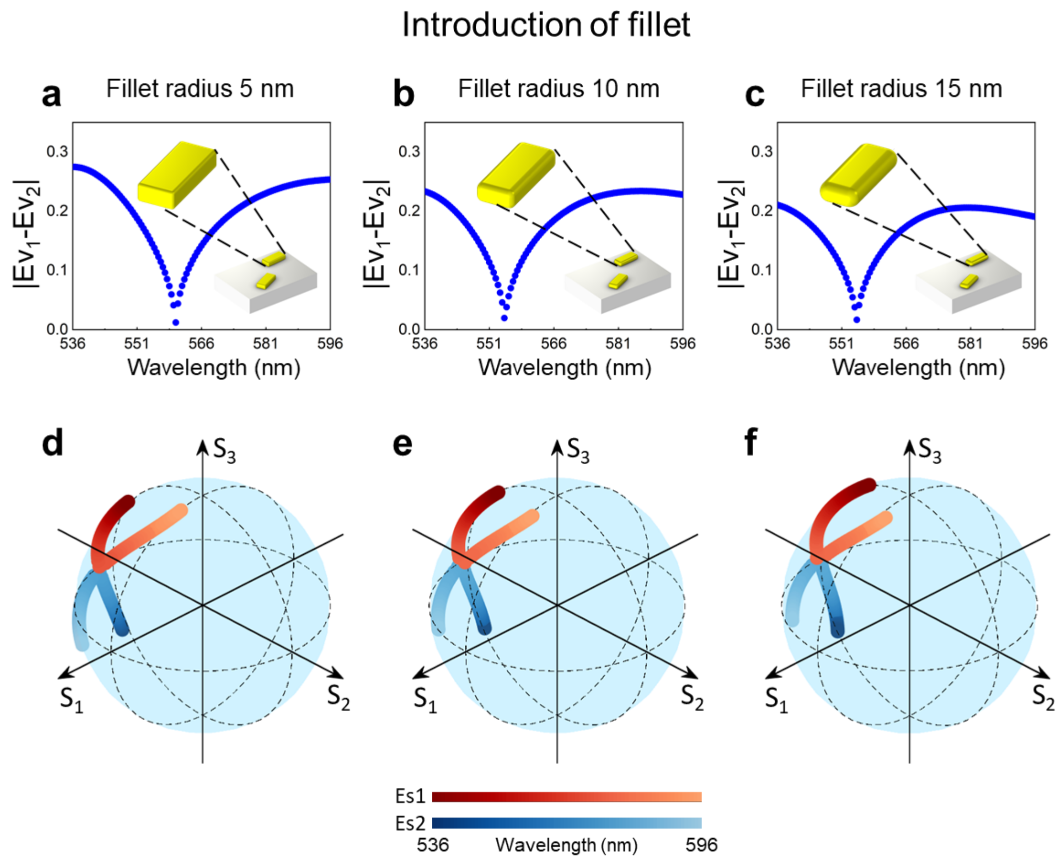

Fig. S12. Impact of fillet radius of nanorods on the existence of EP and its eigenpolarization. a-c, Schematic and spectrum of EPs. $Ev_{1,2}$ are the eigenvalues of Jones matrix. $|Ev_1 - Ev_2| = 0$ represents the degeneracy of the two eigenvalues. The corresponding shapes are indicated as insets. **d-f,** The corresponding eigenpolarization. The length and width of the two nanorods are $(L, w) = (140\ \mathrm{nm}, 60\ \mathrm{nm})$. The orientation angles of the two nanorods are $(\beta_1, \beta_2) = (26°, 6°)$ and the incident angles are $(\alpha, \theta) = (0°, 60°)$.

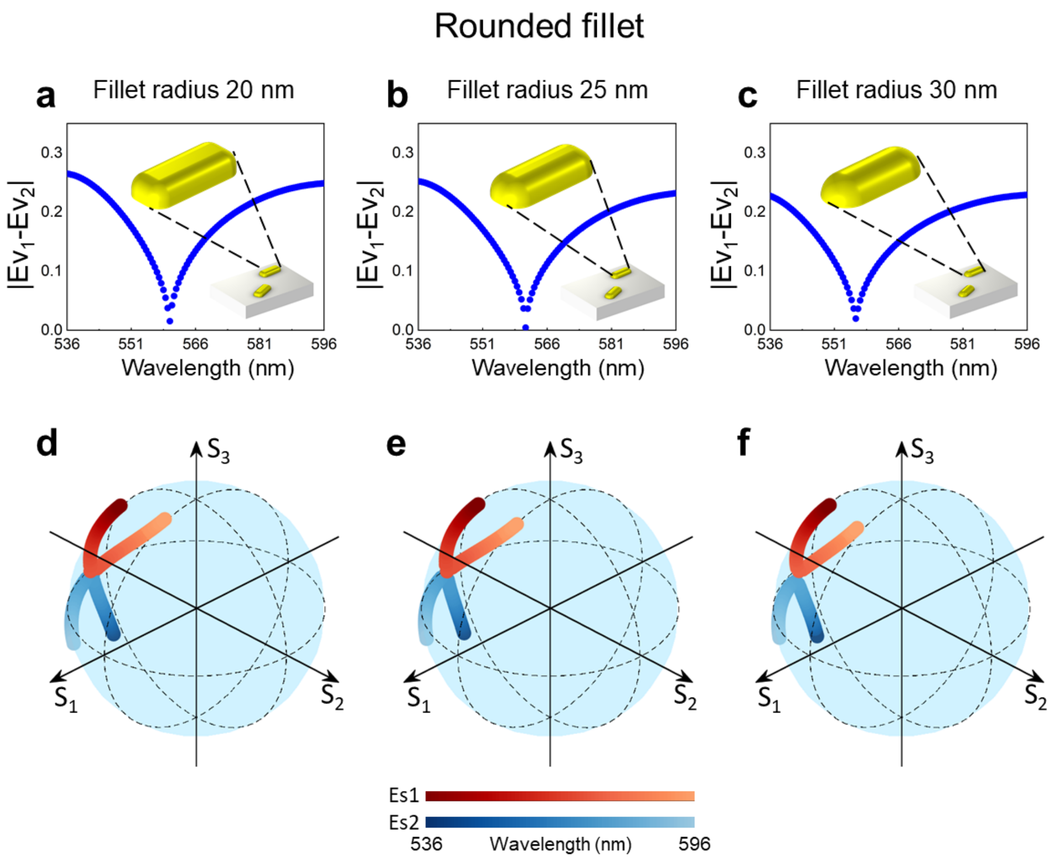

Fig. S13. Impact of largely rounded fillet radius of nanorods on the existence of EP and its eigenpolarization. a-c, Schematic and spectrum of EPs. $Ev_{1,2}$ are the eigenvalues of Jones matrix. $|Ev_1 - Ev_2| = 0$ represents the degeneracy of the two eigenvalues. The corresponding shapes are indicated as insets. **d-f,** The corresponding eigenpolarization. The length and width of the two nanorods are $(L, w) = (140\text{ nm}, 60\text{ nm})$. The orientation angles of the two nanorods are $(\beta_1, \beta_2) = (26°, 6°)$ and the incident angles are $(\alpha, \theta) = (0°, 60°)$.

The fillet radius is then increased to a very extreme case that deforms the two nanorods, that resemble half cylinders (Fig. S13). The EP still exists as shown by the zero point of absolute difference between two eigenvalues. The corresponding wavelength of EP is slightly shifted to shorter wavelength.

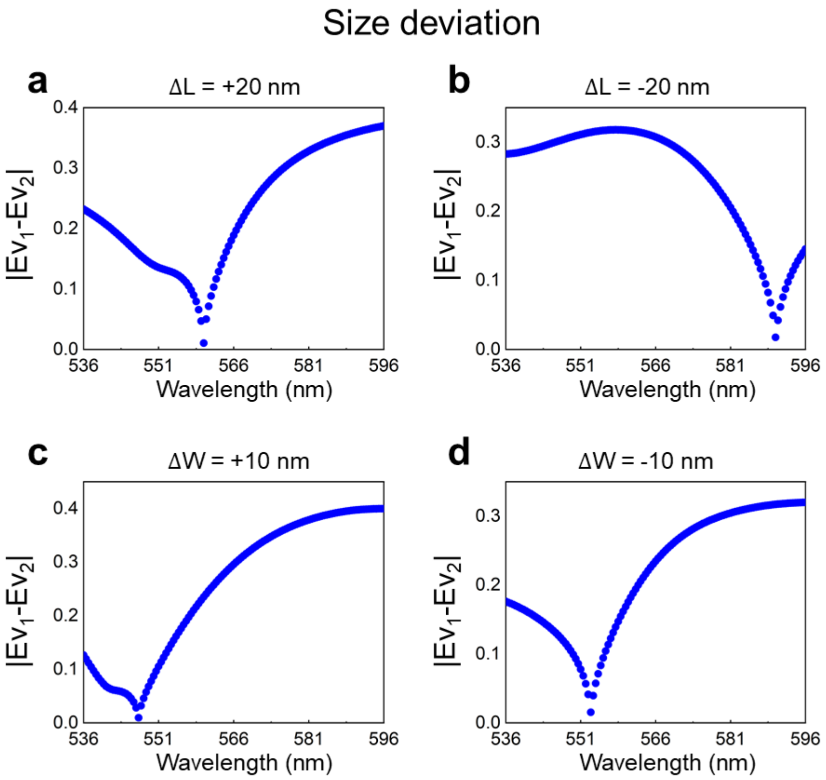

Fig. S14. Impact of size deviation of nanorods on the existence of EP and its eigenpolarization. Spectra of EPs with (**a,b**) length deviation of $\Delta L = +20\text{ nm}$ and $\Delta L = -20\text{ nm}$, (**c,d**) width deviation of $\Delta w = +10$ nm and $\Delta w = -10\text{ nm}$. $Ev_{1,2}$ are the eigenvalues of Jones matrix. $|Ev_1 - Ev_2| = 0$ represents the degeneracy of the two eigenvalues. The original length and width of the two nanorods are $(L, w) = (140\text{ nm}, 60\text{ nm})$. The orientation angles of the two nanorods are $(\beta_1, \beta_2) = (26°, 6°)$ and the incident angles are $(\alpha, \theta) = (0°, 60°)$. ΔL and Δw represents the size deviation of the length L and the width w, respectively.

We also consider the size deviation of nanorods in Fig. S14. By changing the length and width of the two nanorods, we confirm that the existence of arbitrary EP is robust against the fabrication imperfection in the size.

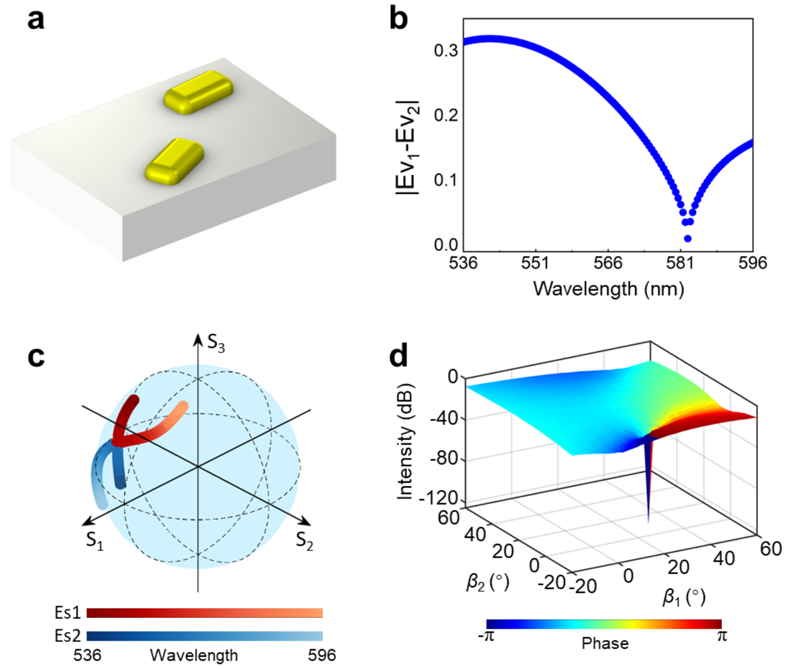

Fig. S15. Rounded fillet of nanorods and its EP, eigenpolarization, and EP induced topological phase. a, Schematic layout of the unit cell. **b,** Spectrum of EP. **c,** The corresponding eigenpolarization. **d,** Topological phase distribution in parameter space around EP. To mimic the actual device, the shape is set as $(L, w) = (130\text{ nm}, 70\text{ nm})$ with rounded fillet for fabrication imperfection. $Ev_{1,2}$ are the eigenvalues of Jones matrix. The color in (**c**) corresponds to wavelength from minimum to maximum.

The topological phase is also analyzed by applying the rounded fillet in the nanorods as shown in Fig. S15. The geometry of the nanorod is modified according to the measured results from SEM image in Fig. 4a and 5a of the main text. We find that the existence of such arbitrary EP and topological phase is robust.

References

1. Deng, Z. L. *et al.* Full-color complex-amplitude vectorial holograms based on multi-freedom metasurfaces. *Adv. Funct. Mater.* **30**, 1910610 (2020).
2. Deng, Z. L. *et al.* Vectorial compound metapixels for arbitrary nonorthogonal polarization steganography. *Adv. Mater.* **33**, 2103472 (2021).
3. Yun, G., Crabtree, K. & Chipman, R. A. Three-dimensional polarization ray-tracing calculus I: definition and diattenuation. *Appl. Optics* **50**, 2855-2865 (2011).
4. Özdemir, Ş. K., Rotter, S., Nori, F. & Yang, L. Parity–time symmetry and exceptional points in photonics. *Nat. Mater.* **18**, 783-798 (2019).
5. Peterson, C. W., Kim, S., Bernhard, J. T. & Bahl, G. Synthetic phonons enable nonreciprocal coupling to arbitrary resonator networks. *Sci. Adv.* **4**, eaat0232 (2018).
6. Zhang, L. *et al.* Acoustic non-Hermitian skin effect from twisted winding topology. *Nat. Commun.* **12**, 6297 (2021).
7. Sounas, D. L. & Alù, A. Non-reciprocal photonics based on time modulation. *Nat. Photonics* **11**, 774-783 (2017).
8. Zhang, X.-L., Jiang, T. & Chan, C. T. Dynamically encircling an exceptional point in anti-parity-time symmetric systems: asymmetric mode switching for symmetry-broken modes. *Light Sci. Appl.* **8**, 88 (2019).
9. Peng, B. *et al.* Chiral modes and directional lasing at exceptional points. *Proc. Natl Acad. Sci. USA* **113**, 6845-6850 (2016).
10. Miri, M.-A. & Alu, A. Exceptional points in optics and photonics. *Science* **363**, eaar7709 (2019).
11. Nasari, H. *et al.* Observation of chiral state transfer without encircling an exceptional point. *Nature* **605**, 256-261 (2022).
12. Wang, C., Sweeney, W. R., Stone, A. D. & Yang, L. Coherent perfect absorption at an exceptional point. *Science* **373**, 1261-1265 (2021).
13. Huang, Y., Shen, Y., Min, C., Fan, S. & Veronis, G. Unidirectional reflectionless light propagation at exceptional points. *Nanophotonics* **6**, 977-996 (2017).
14. Ding, K., Fang, C. & Ma, G. Non-Hermitian topology and exceptional-point geometries. *Nat. Rev. Phys.* **4**, 745-760 (2022).
15. Zhou, Z., Jia, B., Wang, N., Wang, X. & Li, Y. Observation of perfectly-chiral exceptional point via bound state in the continuum. *Phys. Rev. Lett.* **130**, 116101 (2023).